Flavour Hund's Coupling, Chern Gaps, and Charge Diffusivity in Moiré Graphene

Jeong Min Park[1,*], Yuan Cao[1,*,†], Kenji Watanabe[2], Takashi Taniguchi[3], Pablo Jarillo-Herrero[1,†]

[1]Department of Physics, Massachusetts Institute of Technology, Cambridge, Massachusetts 02139, USA

[2]Research Center for Functional Materials, National Institute for Materials Science, Namiki 1-1, Tsukuba, Ibaraki 305-0044, Japan

[3]International Center for Materials Nanoarchitectonics, National Institute for Materials Science, Namiki 1-1, Tsukuba, Ibaraki 305-0044, Japan

*These authors contributed equally.

†Correspondence to: caoyuan@mit.edu, pjarillo@mit.edu

Interaction-driven spontaneous symmetry breaking lies at the heart of many quantum phases of matter. In moiré systems, broken spin/valley 'flavour' symmetry in flat bands underlies the parent state from which ultimately correlated and topological ground states emerge[1–10]. However, the microscopic mechanism of such flavour symmetry breaking and its connection to the low-temperature phases remain to be understood. Here, we investigate the broken-symmetry many-body ground state of magic-angle twisted bilayer graphene (MATBG) and its nontrivial topology using simultaneous thermodynamic and transport measurements. We directly observe flavour symmetry breaking as a pinning of the chemical potential at all integer fillings of the moiré superlattice, highlighting the importance of flavour Hund's coupling in the many-body ground state. The topological nature of the underlying flat bands is manifested upon breaking time-reversal symmetry, where we measure energy gaps corresponding to Chern insulator states with Chern numbers $C = 3, 2, 1$ at filling factors ν=1,2,3, respectively, consistent with flavour symmetry breaking in the Hofstadter's butterfly spectrum of MATBG. Moreover, concurrent measurements of resistivity and chemical potential allow us to obtain the temperature-dependent charge diffusivity of MATBG in the strange metal regime[11], a quantity previously explored only in ultracold atoms[12]. Our results bring us one step closer to a unified framework for understanding interactions in the topological bands of MATBG, with and without a magnetic field.

In condensed matter systems with flat electronic bands, the Coulomb interaction between electrons can easily surpass their kinetic energy and give rise to a variety of exotic quantum phases, including Mott insulators, quantum spin liquids, and Wigner crystals[13–15]. In this strongly correlated regime, electrons may spontaneously order themselves to minimize the total Coulomb energy at the cost of increasing their kinetic energies, leading to the breaking of certain symmetries. Such broken-symmetry states can occur at a relatively high energy scale and act as a parent state for phases that appear at lower energy scales, such as superconductivity. Furthermore, when there is nontrivial topology in the system, the interplay between strong correlations and the underlying topology could lead to novel phases of matter. Understanding the

physics behind this interplay could guide us in designing next-generation strongly-correlated topological quantum materials.

Magic-angle twisted bilayer graphene (MATBG) serves as a unique platform to investigate interaction driven phenomena in a highly tunable flat-band system. When two layers of monolayer graphene (MLG) are stacked with a small twist angle of $\theta \sim 1.1°$, the interlayer hybridization in the resulting moiré superlattice renormalizes the Fermi velocity and creates flat bands at low energies[16,17]. In this regime, a plethora of exotic correlated and topological phenomena have been experimentally demonstrated, including correlated insulator states, superconductivity, and the quantum anomalous Hall effect[1,2,4–7]. Scanning tunneling and single-electron transistor experiments have directly shown the significance of Coulomb-induced phase transitions that break the spin/valley symmetry[9,10,18–21]. Despite significant experimental and theoretical progress, the microscopic picture that underlies the broken-symmetry states and their possible connections to the correlated phases and superconductivity still requires investigation.

Flavour Hund's Coupling in MATBG

Here we study the interplay between interaction-driven symmetry breaking and nontrivial topology in MATBG by directly measuring the combined thermodynamic and transport properties of its many-body ground state. We use a unique technique[22] to sense the chemical potential of MATBG. The MATBG is separated from a MLG layer by an ultrathin layer of hBN ($\sim$ 1 nm, Fig. 1a). We use the top gate voltage V_{tg} and back gate voltage V_{bg} to control the densities in MLG and MATBG, and measure the transport properties of the two layers simultaneously. Direct probing of the chemical potential μ of one layer is achieved by sensing the screening of the electric field from the gates by the other layer[22] (Fig. 1b and Supplementary Information). In particular, when one layer is at the charge neutrality point (CNP), e.g. $n_{MLG} = 0$, the chemical potential of the other layer (μ_{MATBG}) is given by $\mu_{MATBG} = -\left(\frac{eC_{tg}}{C_i}\right)V_{tg}$, where C_{tg} and C_i are the geometric capacitances per unit area of the top and middle hBN dielectrics, respectively.

The MLG layer used in our experiments has very low disorder $< 3 \times 10^9$ cm^{-2} (Fig. 1c). The MATBG layer has a twist angle of $\theta = 1.07 \pm 0.03°$, and exhibits correlated states at integer filling factors $\nu_{MATBG} = \frac{4n_{MATBG}}{n_s} = +1, \pm 2, +3$ of the flat bands ($n_s = 8\theta^2/\sqrt{3}a^2$ is the superlattice density of TBG and a=0.246 nm is the graphene lattice constant), as well as superconducting states at both $\nu = -2 - \delta$ and $+2 + \delta$, where δ is a small change in filling (Fig. 1d). The superconducting transition temperature T_c reaches as high as 2.7 K for $\nu = -2 - \delta$ (Extended Data Figure 1). Figure 1e and f show the resistance of MATBG and MLG as a function of V_{tg} and V_{bg} at $B_\perp$=0 T and $B_\perp$=1 T, respectively. As a proof of principle, μ_{MLG} as a function of n_{MLG} is obtained by tracking the CNP of MATBG (Fig. 1e inset and Supplementary Information), from which we determine the MLG Fermi velocity to be $v_F = 1.12 \times 10^6$ m/s by fitting to $|\mu_{MLG}| = \hbar v_F \sqrt{\pi |n_{MLG}|}$. In a magnetic field $B_\perp = 1$ T, the spectrum of MLG is quantized into discrete Landau levels at energies $\pm v_F \sqrt{2e\hbar B|N|}$ as expected. Our technique can thus determine the chemical potential of either layer with a sensitivity of $\lesssim$ 1 meV.

The chemical potential of MATBG is shown in Fig. 2a. Hereafter we will simply use n (ν) and μ to denote n_{MATBG} (ν_{MATBG}) and μ_{MATBG}. The V_{tg} axis is directly proportional to μ when tracking

the CNP of MLG (shown as the green curve). The longitudinal resistance R_{xx} of MLG (purple) and MATBG (orange) is overlaid for qualitative comparison, and the gray dash lines indicate the integer filling factors $\nu = 0, \pm1, \pm2, \pm3$. Around the MATBG CNP ($\nu = 0$), μ rises quickly with ν, consistent with a minimal DOS at the Dirac point. However, once we start filling electrons into the flat band, its slope decreases quickly and μ reaches a local maximum around $\nu = 0.6$. Surprisingly, it then decreases, exhibiting a negative inverse compressibility $\chi^{-1} = d\mu/dn$,[23] and gets pinned at a local minimum around $\nu = 1$. Subsequently, μ rises again until it reaches the next maximum. This intriguing pinning behaviour repeats at each integer filling factor, including $\nu = 4$ (Fig. 2a inset). On the hole-doped side ($\nu < 0$), the pinning behaviour is opposite and weaker (*i.e.* creates weak maxima in μ). The total bandwidth estimated from μ is around ~40 meV. We also investigated μ versus temperature from 2 K to 70 K (Fig. 2d). The observed pinning behaviour persists prominently up to 20 K. We point out that the pinning of μ should not be interpreted as a measure of the gaps of the insulator states because its energy scale (visible up to 70 K) is much greater than the typical energy scale of the insulator states (typically below 10 K). Instead, the insulator state, and possibly also the superconducting state, might be thought of as low-energy states that emerge from the broken flavour symmetry 'parent' states. We also note that the pinning on the hole-doped side occurs at slightly more negative values of ν (Supplementary Information).

The pinning of μ at all integer ν is reminiscent of the stabilization of half-filled or full-filled electronic shells in atoms, which is known as Hund's rule for maximum spin multiplicity and stems from the Coulomb exchange interaction between the electrons. In MATBG, the pinning behaviour of the chemical potential is naturally explained when both the on-site inter-flavour Coulomb repulsion energy *U* and inter-site intra-flavour exchange energy *J* are considered. We focus on $\nu > 0$ in the following description. Figure 2b shows μ calculated with a mean-field model for different values of *U* and *J* (Supplementary Information), which qualitatively reproduces the experimentally measured μ only when both *U* and *J* are nonzero and of similar magnitude (purple solid curve), beyond the currently established understanding[9,10,21]. A possible mechanism for such stabilization of μ at $\nu = 1$ is illustrated in Fig. 2c and elaborated in the Methods. We note that the mean-field treatment of the Coulomb interactions correctly captures the many-body compressibility to leading order[24], but might not give the same ground state as the exact solution. Other mechanisms, such as the formation of a Wigner crystal[25], might also be relevant to the observation of negative compressibility.

To probe the magnetic properties of the correlated states, we measured μ as a function of in-plane magnetic field up to 11 T (Fig. 2e,f for $\nu = +1$ and $\nu = +2$ and Extended Data Figure 2 for $\nu = -1, -2, +3$). At $\nu = \pm1$, the pinning of μ is clearly strengthened by $B_{\parallel}$, as is the peak in R_{xx}^{MATBG} (Methods and Extended Data Figure 3), suggesting that the $\nu = \pm1$ states develop a spin-polarization in response to the magnetic field. To confirm this, we directly obtained the magnetization by integrating the Maxwell's relation[10] (Fig. 2e inset). We indeed find that the magnetization reaches a value on the order of one μ_B at $\nu = \pm1$, consistent with a spin-polarized state at finite field, which would indicate either a very soft paramagnetic state or a ferromagnetic state at zero field. The $\nu = \pm2$ states, on the other hand, have been speculated to be spin-unpolarized insulating states[1,4,26]. However, we find that, while the transport peak there is indeed suppressed by $B_{\parallel}$ (see Fig. 2f and Extended Data Figure 3), μ measured at $\nu = \pm2$ does not show significant dependence on the in-plane magnetic field (Fig. 2f). Furthermore, $M_{\parallel}$ does not return to zero when ν is tuned from ±1 to ±2 (Fig. 2e inset). While the lack of dependence of μ can be

partially captured by our theoretical model (Supplementary Information), the persistence of magnetization near $\nu = \pm 2$ is at odds with the finite-field spin-unpolarized ground state inferred from transport. These observations suggest that in an in-plane field the $\nu = \pm 2$ gaps might select a ground state with nontrivial spin and/or valley texture, beyond simply occupying two flavours with opposite spins.

Our experiments also constrain the possible mechanism of superconductivity in MATBG. The superconducting dome lies in the region where χ^{-1} is high (Extended Data Figure 4b), with maximum T_c corresponding to a maximum in χ^{-1}. Since a Bardeen-Cooper-Schrieffer (BCS) type superconductivity in the weak-coupling limit would be enhanced when the DOS is high (and thus χ^{-1} low), our observation of an opposite trend indicates that it is hard to reconcile the superconductivity in MATBG with a weakly-coupled BCS theory. Future theories attempting to model the superconductivity in MATBG will likely need to consider the importance of Coulomb interactions, including both repulsion and Hund's coupling, and the consequent phase transitions.

Correlated Chern Insulators

We now turn to the topological properties of MATBG. By measuring μ in a perpendicular magnetic field, we can observe the energy gaps that result from the interplay between the Hofstadter spectrum and the Coulomb interactions[26–30]. The helical nature of the Dirac electrons in graphene endows each flat band of MATBG a Chern number of $C = \pm 1$, which is usually explicitly manifested when the composite $C_2\mathcal{T}$ symmetry is broken, either by alignment to the hBN substrate (breaks C_2) or by applying a magnetic field (breaks $\mathcal{T}$). Figure 3c shows the Hofstadter butterfly spectrum of TBG, where the topologically nontrivial gaps ($C = \pm 1$) and the trivial gaps ($C = 0$) are shown. The former gaps are smoothly connected to the Landau level gaps at $\nu_{LL} = \nu/(\phi/\phi_0) = \pm 4$ at low fields, where ϕ is the magnetic flux per unit cell and $\phi_0 = h/e$ is the flux quantum. Without interactions, the only possible total Chern number in this picture is $C_{tot} = 0, \pm 4$, since all flavours are in the same gap. The Coulomb interactions cause their Chern numbers to be different, and give rise to new hierarchies of Chern gaps.

These topological gaps are directly observed in Fig. 3a. Near charge neutrality, we observe the gaps as steps in μ at the Landau level filling factors $\nu_{LL} = 0, \pm 2, \pm 4$, whose positions evolve according to the Streda formula[31] $dn/dB = \nu_{LL}/\phi_0$. In the meantime, the extrema of μ at $\nu = 1, 2, 3$ at $B_\perp = 0$ evolve into topological gaps at $B_\perp = 6$ T. Their evolution follows the same Streda formula $dn/dB = C/\phi_0$ that indicates the total Chern number of $C = 3,2,1$ associated with the states originally at $\nu = 1,2,3$, respectively.

The broken-symmetry Landau levels and topological Chern gaps can be analyzed in a unified way using a correlated Hofstadter spectrum model[32]. We consider the single-particle DOS to be representative of the Hofstadter spectrum shown in Fig. 3c, and add the mean-field *U* and *J* in a similar manner as above. Using this model, we calculate the Chern number C as a function of ν and reproduce the experimentally observed sequence of 0, ±2, ±4 near CNP, and 3, 2, and 1 at densities $\nu = 1 + 3\phi/\phi_0, 2 + 2\phi/\phi_0$, and $3 + \phi/\phi_0$, respectively (Fig. 3d). By performing a similar calculation (Supplementary Information), we can simulate the evolution of the chemical potential with the magnetic field (Fig. 3b). The remarkable similarity with the experimental data clearly indicates that this model captures the main features of the correlated spectrum with and without a magnetic field.

A more quantitative analysis is performed on the chemical potential measured at $B_\perp = 6$ T (Fig. 3e). From the steps in μ, we extract the values of the Landau level gaps at $\nu_{LL} = -4, -2, 0, 2,$ and 4 to be 5.9, 3.3, 5.9, 2.3, and 4.9 meV, respectively. The small values of the gaps at $\nu_{LL} = \pm 4$ translate to a Fermi velocity of approximately $v_F \sim 6 \times 10^4$ m/s, consistent with previous experiments[1,27]. The Chern gaps at $\nu = 1 + 3\phi/\phi_0, 2 + 2\phi/\phi_0$, and $3 + \phi/\phi_0$ are extracted to be 2.2, 5.0 and 1.9 meV respectively. The larger gap at $2 + 2\phi/\phi_0$ is consistent with the fact that this state is more readily resolved in electronic transport experiments[1,2,4,5,26,29]. Its difference with the gaps at $\nu = 1 + 3\phi/\phi_0$ and $3 + \phi/\phi_0$ might be attributed to different magnetic ground states. These gaps have a weak dependence on $B_\perp$ (Extended Data Figure 5), consistent with the Hofstadter spectrum (Fig. 3c).

Charge Diffusivity of a 'Strange Metal'

In correlated metals with multiple bands near the Fermi energy, the atomic Hund's coupling is known to play an important role in their many-body physics, including the strange metal regime[33]. In MATBG, recent experiments have reported evidence for strange metal behaviour[11], manifested as resistivity linear with T from very low T. As shown in Fig. 4a and c, the resistivity in our MATBG sample is largely linear with T over a range of densities around the correlated states, and with a slope that is weakly dependent on n[11,34]. It has been hypothesized that the strange metal behaviour can be universally described by a 'Planckian' scattering rate bound $\Gamma \sim k_B T/\hbar$ in the framework of incoherent non-quasiparticle transport[35]. However, the construction of a microscopic picture for this bound is still in progress[36,37].

A universal framework to investigate the strange metal regime is the Nernst-Einstein relation, which connects the resistivity ρ, compressibility χ, and charge diffusivity D of a generic conductor by $\rho^{-1} = e^2 \chi D$. A linear in T resistivity could thus originate from: (i) $\chi^{-1} \propto T$, which could arise from thermodynamic contributions[38,39] when $k_B T \gtrsim W$; (ii) $D^{-1} \propto T$, which represent a linear scattering rate; or (iii) a combined T-dependence of both. Differentiating between these possibilities could help constrain theoretical models for strange metal behaviour[38,40,41]. However, to the best of our knowledge, there are no reported measurements of the compressibility or charge diffusivity for strange metals, and only recent experiments have begun to explore this physics in ultracold atoms[12].

Our combined resistivity and compressibility measurements allow us to extract the charge diffusivity of MATBG (Fig. 4b). While χ^{-1} becomes negative before each integer filling factor at $T < 20$ K, as discussed above, at higher T it converges to a roughly constant value of order 1 eV·nm^2 regardless of ν. Figure 4d shows selected traces of χ^{-1} vs T, which exhibit only a weak dependence on T, albeit ρ exhibits a prominent linear-in-T behaviour, suggesting that the linear ρ-T behaviour in MATBG is mainly due to a T-dependent charge diffusivity. Figure 4e-f shows the T-dependence of the extracted effective diffusivity $D^* = \chi^{-1}/e^2(\rho - \rho_0)$ and its inverse, where ρ_0 is the residual resistivity extrapolated at zero temperature. These quantities indeed appear to roughly follow a $\sim T^{-1}$ and a $\sim T$ trend, respectively. Our observations therefore indicate that the strange metal regime in MATBG is consistent with a scattering rate linear in T. These arguments do not apply to regions with negative electronic compressibility as the interpretation of diffusivity in this case needs to be modified[42] (Supplementary Information). Interestingly, we find the extracted diffusivity $D^*(T)$ at all these fillings to be within about a factor of 2 from a diffusivity bound $D_{bound} = \hbar v_F^2/(k_B T)$ proposed for incoherent metals[38]. While this bound is known to be violated in the low-temperature region in a large-U system[40],

this is not at odds with our observations if MATBG is in the intermediate U regime ($U/W \sim 1$, deduced from our modeling and other experiments[9,10,18]).

References

1. Cao, Y. *et al.* Correlated insulator behaviour at half-filling in magic-angle graphene superlattices. *Nature* **556**, 80–84 (2018).
2. Cao, Y. *et al.* Unconventional superconductivity in magic-angle graphene superlattices. *Nature* **556**, 43–50 (2018).
3. Chen, G. *et al.* Evidence of a gate-tunable Mott insulator in a trilayer graphene moiré superlattice. *Nat. Phys.* **15**, 237 (2019).
4. Yankowitz, M. *et al.* Tuning superconductivity in twisted bilayer graphene. *Science* **363**, 1059–1064 (2019).
5. Lu, X. *et al.* Superconductors, orbital magnets and correlated states in magic-angle bilayer graphene. *Nature* **574**, 653–657 (2019).
6. Sharpe, A. L. *et al.* Emergent ferromagnetism near three-quarters filling in twisted bilayer graphene. *Science* **365**, 605–608 (2019).
7. Serlin, M. *et al.* Intrinsic quantized anomalous Hall effect in a moiré heterostructure. *Science* **367**, 900–903 (2020).
8. Chen, G. *et al.* Tunable correlated Chern insulator and ferromagnetism in a moiré superlattice. *Nature* **579**, 56–61 (2020).
9. Wong, D. *et al.* Cascade of electronic transitions in magic-angle twisted bilayer graphene. *Nature* **582**, 198–202 (2020).
10. Zondiner, U. *et al.* Cascade of phase transitions and Dirac revivals in magic-angle graphene. *Nature* **582**, 203–208 (2020).
11. Cao, Y. *et al.* Strange Metal in Magic-Angle Graphene with near Planckian Dissipation. *Phys. Rev. Lett.* **124**, 076801 (2020).
12. Brown, P. T. *et al.* Bad metallic transport in a cold atom Fermi-Hubbard system. *Science* **363**, 379–382 (2019).
13. Lee, P. A., Nagaosa, N. & Wen, X.-G. Doping a Mott insulator: Physics of high-temperature superconductivity. *Rev. Mod. Phys.* **78**, 17–85 (2006).
14. Balents, L. Spin liquids in frustrated magnets. *Nature* **464**, 199–208 (2010).
15. Tanatar, B. & Ceperley, D. M. Ground state of the two-dimensional electron gas. *Phys. Rev. B* **39**, 5005–5016 (1989).
16. Suárez Morell, E., Correa, J. D., Vargas, P., Pacheco, M. & Barticevic, Z. Flat bands in slightly twisted bilayer graphene: Tight-binding calculations. *Phys. Rev. B* **82**, 121407 (2010).
17. Bistritzer, R. & MacDonald, A. H. Moiré bands in twisted double-layer graphene. *Proc. Natl. Acad. Sci.* **108**, 12233–12237 (2011).
18. Xie, Y. *et al.* Spectroscopic signatures of many-body correlations in magic-angle twisted bilayer graphene. *Nature* **572**, 101–105 (2019).
19. Kerelsky, A. *et al.* Maximized electron interactions at the magic angle in twisted bilayer graphene. *Nature* **572**, 95–100 (2019).
20. Jiang, Y. *et al.* Charge order and broken rotational symmetry in magic-angle twisted bilayer graphene. *Nature* **573**, 91–95 (2019).

21. Choi, Y. *et al.* Electronic correlations in twisted bilayer graphene near the magic angle. *Nat. Phys.* **15**, 1174–1180 (2019).
22. Kim, S. *et al.* Direct Measurement of the Fermi Energy in Graphene Using a Double-Layer Heterostructure. *Phys. Rev. Lett.* **108**, 116404 (2012).
23. Eisenstein, J. P., Pfeiffer, L. N. & West, K. W. Compressibility of the two-dimensional electron gas: Measurements of the zero-field exchange energy and fractional quantum Hall gap. *Phys. Rev. B* **50**, 1760–1778 (1994).
24. Setiawan, F. & Das Sarma, S. Temperature-dependent many-body effects in Dirac-Weyl materials: Interacting compressibility and quasiparticle velocity. *Phys. Rev. B* **92**, 235103 (2015).
25. Padhi, B., Setty, C. & Phillips, P. W. Doped Twisted Bilayer Graphene near Magic Angles: Proximity to Wigner Crystallization, Not Mott Insulation. *Nano Lett.* **18**, 6175–6180 (2018).
26. Wu, S., Zhang, Z., Watanabe, K., Taniguchi, T. & Andrei, E. Y. Chern Insulators and Topological Flat-bands in Magic-angle Twisted Bilayer Graphene. *ArXiv200703735 Cond-Mat* (2020).
27. Tomarken, S. L. *et al.* Electronic Compressibility of Magic-Angle Graphene Superlattices. *Phys. Rev. Lett.* **123**, 046601 (2019).
28. Nuckolls, K. P. *et al.* Strongly correlated Chern insulators in magic-angle twisted bilayer graphene. *Nature* **588**, 610–615 (2020).
29. Saito, Y. *et al.* Hofstadter subband ferromagnetism and symmetry broken Chern insulators in twisted bilayer graphene. *ArXiv200706115 Cond-Mat* (2020).
30. Das, I. *et al.* Symmetry broken Chern insulators and magic series of Rashba-like Landau level crossings in magic angle bilayer graphene. *ArXiv200713390 Cond-Mat* (2020).
31. Streda, P. & Smrcka, L. Thermodynamic derivation of the Hall current and the thermopower in quantising magnetic field. *J. Phys. C Solid State Phys.* **16**, L895–L899 (1983).
32. Hofstadter, D. R. Energy levels and wave functions of Bloch electrons in rational and irrational magnetic fields. *Phys. Rev. B* **14**, 2239–2249 (1976).
33. Georges, A., Medici, L. de' & Mravlje, J. Strong Correlations from Hund's Coupling. *Annu. Rev. Condens. Matter Phys.* **4**, 137–178 (2013).
34. Polshyn, H. *et al.* Large linear-in-temperature resistivity in twisted bilayer graphene. *Nat. Phys.* **15**, 1011–1016 (2019).
35. Bruin, J. a. N., Sakai, H., Perry, R. S. & Mackenzie, A. P. Similarity of Scattering Rates in Metals Showing T-Linear Resistivity. *Science* **339**, 804–807 (2013).
36. Chowdhury, D., Werman, Y., Berg, E. & Senthil, T. Translationally Invariant Non-Fermi-Liquid Metals with Critical Fermi Surfaces: Solvable Models. *Phys. Rev. X* **8**, 031024 (2018).
37. Patel, A. A. & Sachdev, S. Theory of a Planckian Metal. *Phys. Rev. Lett.* **123**, 066601 (2019).
38. Hartnoll, S. A. Theory of universal incoherent metallic transport. *Nat. Phys.* **11**, 54–61 (2015).
39. Perepelitsky, E. *et al.* Transport and optical conductivity in the Hubbard model: A high-temperature expansion perspective. *Phys. Rev. B* **94**, 235115 (2016).
40. Pakhira, N. & McKenzie, R. H. Absence of a quantum limit to charge diffusion in bad metals. *Phys. Rev. B* **91**, 075124 (2015).
41. Kokalj, J. Bad-metallic behavior of doped Mott insulators. *Phys. Rev. B* **95**, 041110 (2017).

42. Efros, A. L. Negative density of states: Screening, Einstein relation, and negative diffusion. *Phys. Rev. B* **78**, 155130 (2008).

Acknowledgements

The authors thank Sankar Das Sarma, Antoine Georges, Francisco Guinea, Shahal Ilani, Aharon Kapitulnik, Leonid Levitov, Louis Taillefer, Senthil Todadri, Ashvin Vishwanath, Amir Yacoby, Denis Bandurin, Sergio de la Barrera, Clement Collignon, Ali Fahimniya, Daniel Rodan-Legrain, Yonglong Xie, and Kenji Yasuda for fruitful discussions.

This work has been primarily supported by the US Department of Energy (DOE), Office of Basic Energy Sciences (BES), Division of Materials Sciences and Engineering under Award DE-SC0001819 (J.M.P.). Help with transport measurements and data analysis were supported by the National Science Foundation (DMR-1809802), and the STC Center for Integrated Quantum Materials (NSF Grant No. DMR-1231319) (Y.C.). P.J-H acknowledges support from the Gordon and Betty Moore Foundation's EPiQS Initiative through Grant GBMF9643. PJH acknowledges partial support by the Fundación Ramon Areces. The development of new nanofabrication and characterization techniques enabling this work has been supported by the US DOE Office of Science, BES, under award DE-SC0019300. K.W. and T.T. acknowledge support from the Elemental Strategy Initiative conducted by the MEXT, Japan, Grant Number JPMXP0112101001, JSPS KAKENHI Grant Numbers JP20H00354 and the CREST(JPMJCR15F3), JST. This work made use of the Materials Research Science and Engineering Center Shared Experimental Facilities supported by the National Science Foundation (DMR-0819762) and of Harvard's Center for Nanoscale Systems, supported by the NSF (ECS-0335765).

Author Contributions

J.M.P. and Y.C. fabricated the samples, and performed transport measurements and numerical simulations. K.W. and T.T. provided hBN samples. J.M.P., Y.C., and P.J-H. performed data analysis, discussed the results, and wrote the manuscript with input from all co-authors.

Author Information

The authors declare no competing financial interest. Requests for materials and correspondence should be sent to Y.C. (caoyuan@mit.edu) and P.J-H. (pjarillo@mit.edu).

Main Figure Legends

Figure 1. Device structure and demonstration of chemical potential measurement. (a) Schematics of the measurement technique. MATBG and monolayer graphene (MLG) are separated by a thin (~1 nm) hBN spacer and dual-gated. We simultaneously measure the resistance of MATBG and MLG. (b) Band diagram of the heterostructure, showing the

relationship between the chemical potentials of MATBG (μ_{MATBG}) and MLG (μ_{MLG}), the back gate voltage V_{bg} and top gate voltage V_{tg}, and the electrostatic potential drops V_0, V_1, and V_2. e is the electron charge. (c) Transport characterization of MLG, showing a sharp resistance R_{xx}^{MLG} peak versus MLG carrier density n_{MLG}, with full width half maximum of less than 3×10^9 cm^{-2}. Inset: Landau fan diagram (R_{xx}^{MLG} versus n_{MLG} and magnetic field B) in MLG, which shows that the Landau levels become visible already at ±0.03 T. (d) Transport characterization of MATBG. The twist angle of MATBG is $\theta = 1.07 \pm 0.03°$. We find correlated states at filling factors $\nu_{MATBG} = 1, \pm 2, 3$, as well as superconducting domes (blue) at $-2 - \delta$ and $+2 + \delta$, respectively. (e-f) Combined plot of the resistance of MLG and MATBG, represented by purple and orange colour scales, respectively, and overlaid in the same axes. As a proof of principle, we use the charge neutrality point (CNP) of MATBG (orange diagonal feature) to probe the chemical potential of MLG, at (e) B=0 and (f) $B_\perp$ =1 T. The horizontal purple stripes are the resistive features in MLG. From the CNP of MATBG, we extract the chemical potential μ_{MLG} versus density n_{MLG}, which is shown in the insets of (e-f). The white line in the inset of (e) is a fit to $|\mu_{MLG}| = \hbar v_F \sqrt{\pi |n_{MLG}|}$. The red ticks in the inset of (f) denote the expected Landau level (LL) energies $\pm v_F \sqrt{2e\hbar B|N|}$, where $v_F = 1.12 \times 10^6$ m/s and N is an integer.

Figure 2. Chemical potential of MATBG as a function of temperature and in-plane magnetic field. (a) Sensing the chemical potential of MATBG using the CNP of MLG. Measurement taken at B=0 T and T=4 K. The green line shows the extracted chemical potential of MATBG. Gray dash lines mark the integer filling factors of MATBG, which agree with the MATBG correlated resistive features. The chemical potential is pinned at each filling factor, showing the stabilization of the state. The inset shows the same features probed by tracking the N=1 MLG LL at B=0.7 T. (b) Mean-field estimate of the chemical potential with various Coulomb repulsion energy U and exchange energy J in units of the single-particle bandwidth $W \equiv 1$. The experimental data are best explained qualitatively when both terms are nonzero. (c) Illustration of interaction-driven chemical potential stabilization at $\nu = 1$. Chemical potential curve at T=2 K near $\nu = 1$ is shown. A phase transition associated with flavour symmetry breaking occurs before each integer filling factor (except $\nu = 4$). The exchange energy J stabilizes the filled flavour when the filling factor is close to one. (d) Temperature dependence of the chemical potential of MATBG from T=2 K to T=70 K, probed with the MLG CNP. Clear pinning behaviour at integer filling factors persists up to T=20 K. (e) In-plane magnetic field, $B_\parallel$, dependence of the chemical potential of MATBG at T=4 K and $B_\perp$=0.7 T, probed with the N=1 MLG LL. The pinning in chemical potential around odd filling factors $\nu = \pm 1$ gets intensified as $B_\parallel$ is applied, whereas those at filling factors ±2 do not display significant change. Inset: Magnetization $M_\parallel$ in units of Bohr magneton μ_B per moiré unit cell, which shows that all states at $\nu = \pm 1, \pm 2, \pm 3$ are magnetized in an in-plane field. Error bands (blue) correspond to 95% confidence interval. (f) Zoom-in of the chemical potential (top) and transport resistance (bottom) aligned for comparison, shown for $\nu = +1, +2$. The same plots for other fillings are shown in Extended Data Figure 2.

Figure 3. Probing the correlated Chern gaps of MATBG in a perpendicular magnetic field. (a) Experiment and (b) simulation of the chemical potential versus ν in MATBG, at $B_\perp$ from zero to 6 T. W is the bandwidth used in the simulation (see Supplementary Information). Near charge neutrality we find gaps that correspond to Landau level filling factors $\nu_{LL} = 0, \pm 2$, and ± 4, while the pinning of μ at $\nu = 1,2,3$ shown in Fig. 2 evolves into topological gaps with Chern

numbers C=3,2,1, respectively, as evident from their slope in magnetic field $dn/dB = C/\phi_0$, where ϕ_0 is the flux quantum. (c) The Hofstadter's butterfly spectrum of TBG up to a flux per unit cell of $\phi_0/2$ (calculation shown for 1.8°, but spectrum is qualitatively similar for the magic angle). The major gaps in the spectrum have Chern numbers of C=0, -1, +1, 0 per flavour, respectively. (d) Calculated total Chern number of TBG using the mean-field model with Coulomb repulsion and exchange interactions for a flux of $\phi_0/6$. The correct Chern number is reproduced, both in the Landau levels near the charge neutrality (C=-4,-2,0,2,4, indicated by red bars) and in the correlated Chern gaps (C=3,2,1, indicated by the blue bars). The dots above the plot show the configuration of the four flavours in each gap. The colouring scheme of the dots matches the ones shown in (c). Adding the Chern number of each flavour gives the total Chern number. (e) Extraction of energy gaps in the correlated spectrum of MATBG at $B_\perp = 6$ T. See Extended Data Figure 5 for their dependence on $B_\perp$.

Figure 4. Resistivity, electronic compressibility, and diffusivity of MATBG in the strange metal regime. (a) Resistivity and (b) inverse electronic compressibility $\chi^{-1} = d\mu/dn$ of MATBG versus ν and temperature. Colour marks show the position of ν where the line-cuts are taken in (c-f). (c) Linear resistivity-temperature behaviour across a range of densities around the correlated states, with only a weak dependence of slope on ν. (d) Line-cuts of χ^{-1} do not show significant dependence on T. (e) Effective diffusivity $D^* = \chi^{-1}/e^2(\rho - \rho_0)$, where ρ_0 is obtained by fitting the linear in T range and extrapolating to T=0. (f) $1/D^*$ shows linear trend as a function of T. The gray dash line denotes a diffusivity bound $D_{bound}(T) = \hbar v_F^2/(k_B T)$, where we used a Fermi velocity of $v_F = 6 \times 10^4$ m/s.

Methods

Sample Fabrication

The multilayer heterostructure consists of one sheet of monolayer graphene (MLG) and twisted bilayer graphene (TBG) twisted at a small angle $\theta \sim 1.1°$, separated by a thin (~1 nm) hBN layer. This sandwich is encapsulated by two h-BN flakes. All flakes were first exfoliated on SiO_2/Si substrates, and subsequently analyzed with optical microscopy and atomic force microscopy to determine their thicknesses and quality. The multilayer heterostructure was fabricated by a modified polymer-based dry pick-up technique, where a layer of poly(bisphenol A carbonate)(PC)/polydimethylsiloxane(PDMS) on a glass slide fixed on the micro-positioning stage was used to sequentially pick up the flakes. The order of the pick-up was hBN-MLG-hBN(1 nm)-MLG-MLG, where the last two MLG sheets were laser-cut from one MLG flake (see Supplementary Information) and twisted by an angle ~1.1°. All hBN layers were picked up at 90°C, while the MLG layers were picked up at room temperature. The hBN-MLG-hBN(1 nm)-MLG-MLG heterostructure was then released on the pre-stacked hBN-Pd/Au back gate at 175°C. Hall-bar geometry for transport measurements was defined with electron beam lithography and reactive ion etching for each of the MLG and MLG-MLG layers. The top gate and electrical edge-contacts were patterned with electron beam lithography and thermal evaporation of Cr/Au.

Measurement Setup

Electronic transport measurements were performed in a dilution refrigerator with a superconducting magnet, with a base electronic temperature of 70 mK. Current through the sample, amplified by 10^7 V/A, and the four-probe voltage, amplified by 1000, were measured with SR-830 lock-in amplifiers synchronized at the same frequency between 1~20 Hz. Current excitation of 1 nA or voltage excitation of 50~100 μV was used for resistance measurements. We measured both MLG and MATBG layers simultaneously for accurate comparison. See Supplementary Information for details of the extraction of chemical potential from the data.

Flavour Symmetry Breaking and Negative Compressibility at $\nu = 1$

In Fig. 2c, we schematically illustrated the spontaneous flavour symmetry breaking at $\nu = 1$ due to the Coulomb interactions, and how this generates negative compressibility when a finite *J* is present. Near charge neutrality, as the density is increased, all four flavours are filled at the same rate (panel (i)). As ν starts to approach one, the Coulomb repulsion between different flavours starts to surpass the kinetic energy penalty of filling up only one flavour. As ν reaches a certain value (still below 1), a flavour-symmetry-breaking phase transition occurs and all electrons are transferred into a single flavour to minimize the Coulomb repulsion[9,10] (panel (ii)). From this phase transition point all the way to $\nu = 1$, i.e. while a single flavour is being filled, the *U* term does not have any contribution to the free energy, while the *J* term decreases the total free energy as $\sim -J\nu^2$ (see Supplementary Information). This term decreases the chemical potential and results in a negative inverse compressibility $\chi^{-1} \propto \mathcal{D}^{-1} - 2J$ ($\mathcal{D}$ is the single-particle DOS per flavour) when $2J > \mathcal{D}^{-1}$. At $\nu = 1$ (panel (iii)), maximal stabilization by the exchange term *J* is reached, and thus the pinning of μ. Further increase in ν (panel (iv)) populates the other three empty flavours and it increases the chemical potential before the next phase transition occurs.

We note that systems with negative compressibility tend to phase separate in order to minimize the total free energy. The observation of a negative compressibility indicates that our system might be in a strong Coulomb frustration regime[43], which acts to suppress macroscopic phase separation that may occur otherwise in an unconstrained system.

Maxwell's Relations

Using Maxwell's relations between thermodynamic variables, we can obtain information about various thermodynamic quantities by taking different derivatives of the chemical potential. The free energy of the system per unit area in the presence of a magnetization can be written as $g = u - Ts - M_\parallel B_\parallel$, where *u*, *M*, *s* are the internal energy, magnetization, and entropy per area respectively. *u* and *g* satisfy

$$du = Tds + B_\parallel dM_\parallel + \mu d\nu, \quad (1)$$

$$dg = -sdT - M_\parallel dB_\parallel + \mu d\nu. \quad (2)$$

By taking the second derivative of g with respective to (ν, $B_\parallel$) in different orders, we can obtain the following Maxwell's relationship,

$$\left(\frac{\partial M_\parallel}{\partial \nu}\right)_{T,B_\parallel} = -\left(\frac{\partial \mu}{\partial B_\parallel}\right)_{T,\nu}, \quad (3)$$

Therefore, we can integrate from the $B_\parallel$-derivative of μ to obtain the change in $M_\parallel$ as a function of density ν,

$$M_\parallel = M_\parallel(\nu = 0) - \int_0^\nu \left(\frac{\partial \mu}{\partial B_\parallel}\right)_{T,\nu'} d\nu'$$

The extracted $\partial M_\parallel/\partial \nu$ and $M_\parallel$ versus ν are shown in Extended Data Figure 6. We extract the uncertainty (95% confidence interval) of $\partial M_\parallel/\partial \nu$ from fitting of μ with $B_\parallel$, and propagate through the integration to obtain uncertainty in $M_\parallel$.

Thermal activation gap analysis

Thermal activation gap analysis was performed based on the Arrhenius formula $R \sim \exp(-\Delta/2k_BT)$, where k_B is the Boltzmann constant and Δ is the gap size. A temperature-dependent background was removed from the raw resistance R_{xx} of MATBG to avoid being affected by the linear R_{xx}-T behaviour in MATBG[26]. The corrected quantity is denoted by R^*_{MATBG} and shown in Extended Data Fig. 3a-b. By fitting the gaps as a function of the in-plane magnetic field $B_\parallel$ to $\Delta = g\mu_B B_\parallel$, where μ_B is the Bohr magneton, we find effective transport g-factors of ~1.31 for the $\nu = +2$ state and ~0.57 for the $\nu = +1$ state, as shown in Extended Data Fig. 3c.

Methods References

43. Ortix, C., Lorenzana, J. & Di Castro, C. Coulomb-Frustrated Phase Separation Phase Diagram in Systems with Short-Range Negative Compressibility. *Phys. Rev. Lett.* **100**, 246402 (2008).

Data Availability Statement

The data that support the current study are available from the corresponding authors upon reasonable and well-motivated request.

Extended Data Figure Legends

Extended Data Figure 1. Superconductivity and Landau fan diagram of MATBG. (a) Superconducting curves for $\nu = -2 - \delta$ and $+2 + \delta$ domes of MATBG. Maximum T_c~2.7 K is determined from 50% normal resistance of the $\nu = -2 - \delta$ curve. (b) Landau fan diagram of MATBG at 1 K. The CNP shows the main sequence $\nu_{LL} = \pm 4, \pm 8, \ldots$ and broken symmetry states $\nu_{LL} = -1, \pm 2, \pm 3$. There are fans from $\nu = \pm 2$, where the sequence $\nu_{LL} = +2, +4, +6$ and $\nu_{LL} = -2$ are seen, respectively. We also find transport evidence of a correlated Chern gap with Chern number C=3 from $\nu = +1$.

Extended Data Figure 2. In-plane magnetic field dependence of μ and R_{xx} at (a) $\nu = -2$, (b) $\nu = -1$, and (c) $\nu = +3$. (a-b) The hole-doped side features are qualitatively similar to the features on the electron-doped side, but weaker. Note that the 'dip' in μ on the electron-doped side is analogous to the 'peak' on the hole-doped side. For $\nu = -1$, the peak in R_{xx} and the 'peak' feature in μ enhance in $B_\parallel$. For $\nu = -2$, the peak in R_{xx} weakens upon applying $B_\parallel$, while the feature in μ does not exhibit a noticeable change. (c) For $\nu = +3$, the trend in μ is similar to that for $\nu = +1$, i.e. the 'dip' feature is enhanced with $B_\parallel$, though the dependence is generally weaker. There is no noticeable peak in R_{xx} at $\nu = +3$.

Extended Data Figure 3. Thermal activation gap analysis and *g*-factors of the correlated states. (a-b) Fitting of temperature-dependent resistance using the Arrhenius formula $R^* \sim \exp(-\Delta/2k_BT)$ at $\nu = +1, +2$, respectively, for in-plane magnetic fields $B_\parallel$ = 0~11 T. R^* is the background-removed resistance of MATBG. (c) $B_\parallel$-dependence of the thermal activation gap Δ. The extracted *g*-factors are ~0.57, ~1.31 for the $\nu = +1, +2$ states, respectively.

Extended Data Figure 4. Overlaying the inverse compressibility and the superconducting dome, and full-range chemical potential data. (a) Temperature dependence of inverse compressibility $d\mu/dn$ for T=2~70 K at B=0 T. Negative compressibility near $\nu = +1, +2$ persists up to $T \sim 20$ K. (b) Comparison between $d\mu/dn$ and superconducting T_c dome (red points, 20% normal-state resistance) near $\nu = -2 - \delta$. The T_c dome occurs near maximum $d\mu/dn$, which is unexpected within a weak coupling BCS-type mechanism for the superconductivity. (c) Same data as Fig. 2d but showing the chemical potential beyond $\nu = \pm 4$.

Extended Data Figure 5. Perpendicular magnetic field dependence of Landau level and Chern gaps. (a-e) Gap extraction from the chemical potential curves at $B_\perp$ = 0~6 T. (f-g) Magnetic field dependence of (f) the Landau level gaps and (g) the correlated Chern gaps. While the $\nu_{LL} = \pm 4, 0$ Landau level gaps have increasing trend with $B_\perp$, the $\nu_{LL} = \pm 2$ gaps show relatively weak dependence. Similarly, the three correlated Chern gaps also exhibit weak dependence on $B_\perp$. The reason why the Chern gap at $\nu = 2 + 2\phi/\phi_0$ is larger than the other two might be attributed to the difference in their magnetic ground states, with contributions from both orbital and spin degrees of freedom.

Extended Data Figure 6. In-plane magnetization of MATBG. (a) $\left(\frac{\partial M_\parallel}{\partial \nu}\right)_{T,B_\parallel} = -\left(\frac{\partial \mu}{\partial B_\parallel}\right)_{T,\nu}$ versus ν. Peaks are visible near $\nu = \pm 1$. T=4 K. (b) Magnetization $M_\parallel$ from integrating the curve in (a). $M_\parallel$ persists near all filling factors $\nu = \pm 1, \pm 2, \pm 3$. The error bands correspond to a confidence level of 95%.

Figure 1

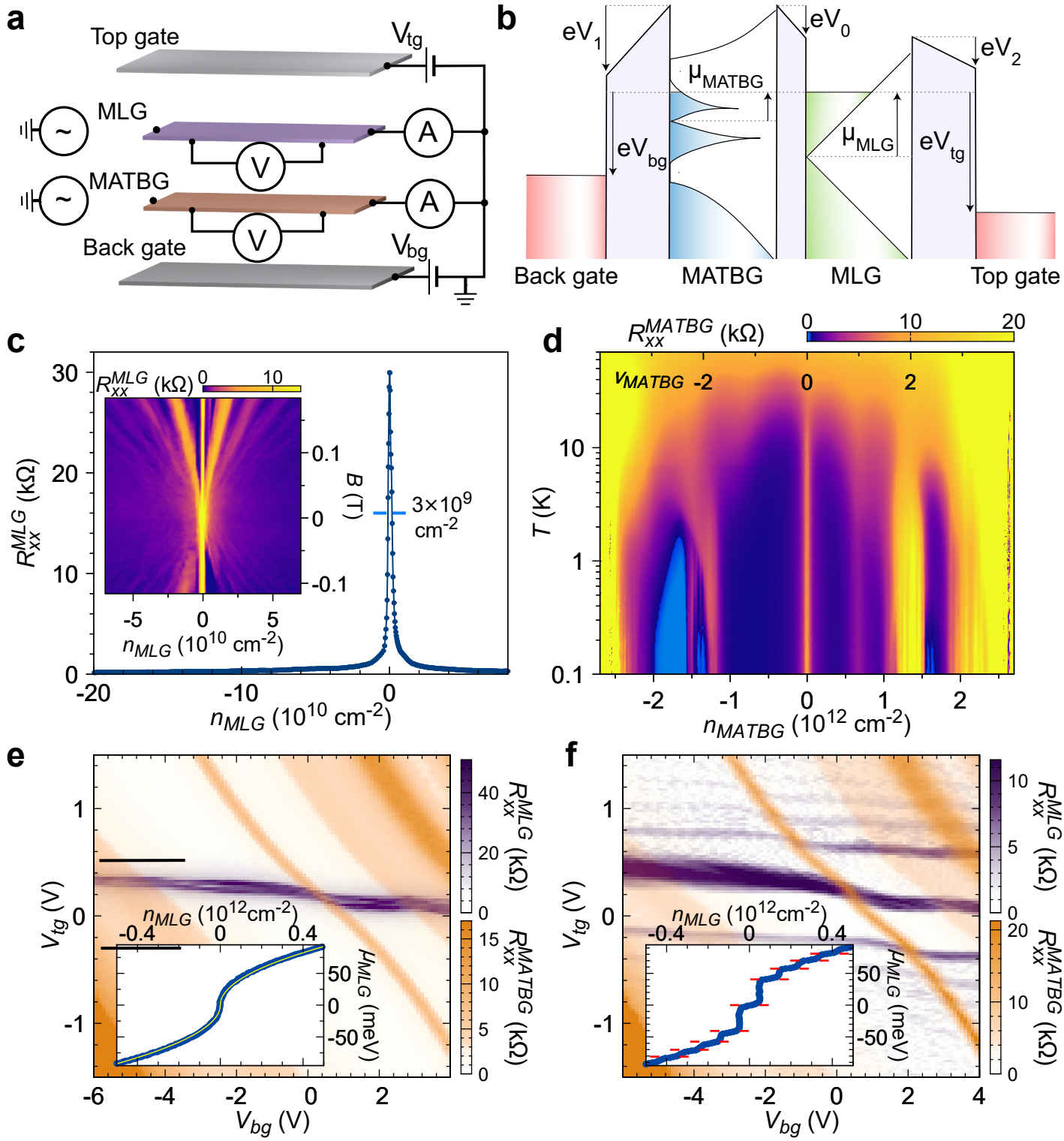
a
Top gate
V_{tg}
MLG
A
V
MATBG
A
V
Back gate
V_{bg}
b
eV_1
eV_0
eV_2
μ_{MATBG}
eV_{bg}
μ_{MLG}
eV_{tg}
Back gate
MATBG
MLG
Top gate
c
R_{xx}^{MLG} (kΩ)
R_{xx}^{MLG} (kΩ)
B (T)
3×10^9 cm^{-2}
n_{MLG} (10^{10} cm^{-2})
n_{MLG} (10^{10} cm^{-2})
d
R_{xx}^{MATBG} (kΩ)
ν_{MATBG}
T (K)
n_{MATBG} (10^{12} cm^{-2})
e
V_{tg} (V)
n_{MLG} (10^{12}cm^{-2})
μ_{MLG} (meV)
R_{xx}^{MLG} (kΩ)
R_{xx}^{MATBG} (kΩ)
V_{bg} (V)
f
V_{tg} (V)
n_{MLG} (10^{12}cm^{-2})
μ_{MLG} (meV)
R_{xx}^{MLG} (kΩ)
R_{xx}^{MATBG} (kΩ)
V_{bg} (V)

Figure 2

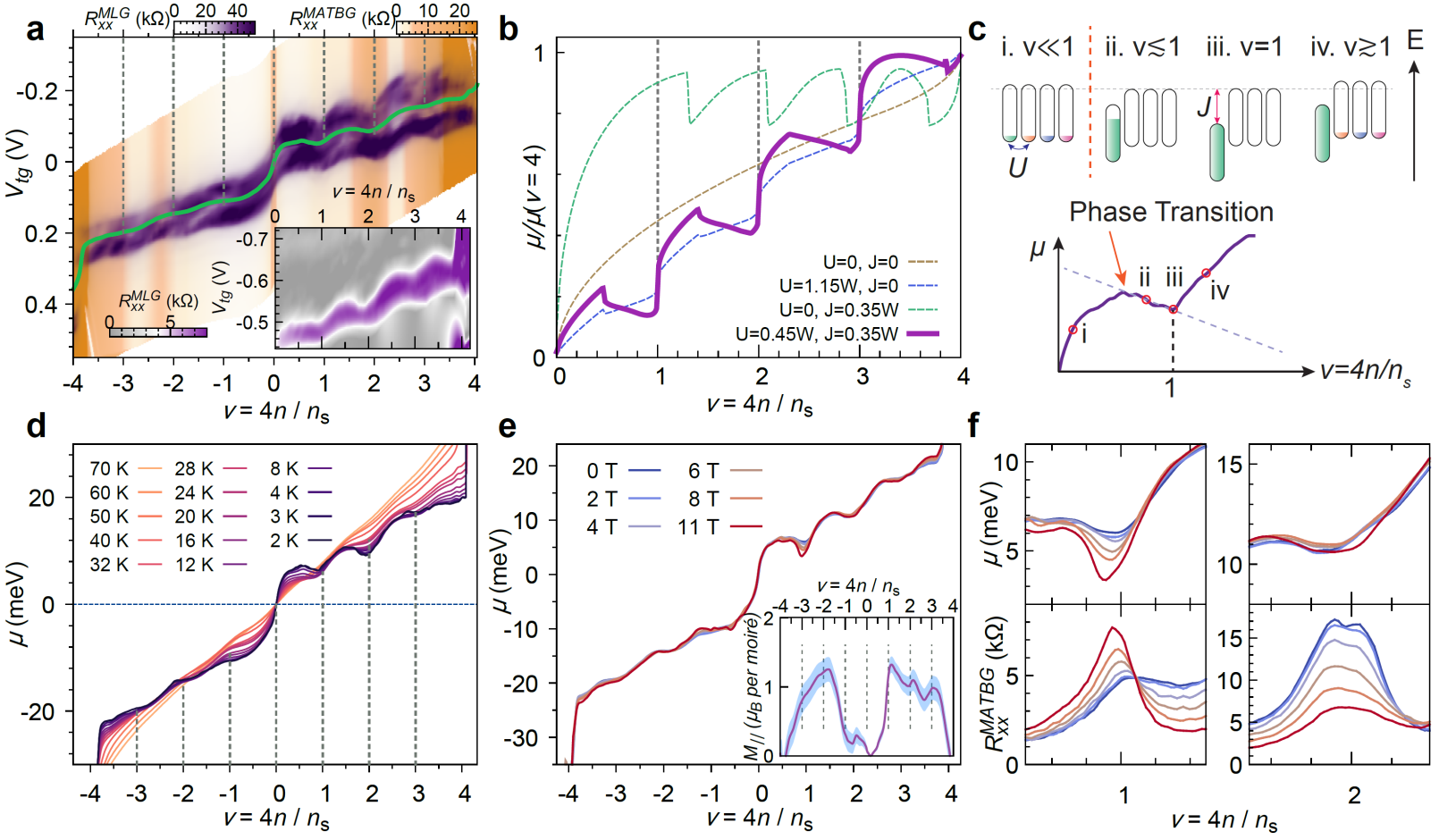
a
b
c
d
e
f
R_{xx}^{MLG} (kΩ)
R_{xx}^{MATBG} (kΩ)
V_{tg} (V)
$\nu = 4n / n_s$
$\mu/\mu(\nu = 4)$
U=0, J=0
U=1.15W, J=0
U=0, J=0.35W
U=0.45W, J=0.35W
i. ν≪1
ii. ν≲1
iii. ν=1
iv. ν≳1
E
U
J
Phase Transition
μ
i
ii
iii
iv
$\nu=4n/n_s$
70 K
60 K
50 K
40 K
32 K
28 K
24 K
20 K
16 K
12 K
8 K
4 K
3 K
2 K
μ (meV)
0 T
2 T
4 T
6 T
8 T
11 T
$M_{//}$ (μ_B per moiré)
R_{xx}^{MATBG} (kΩ)

Figure 3

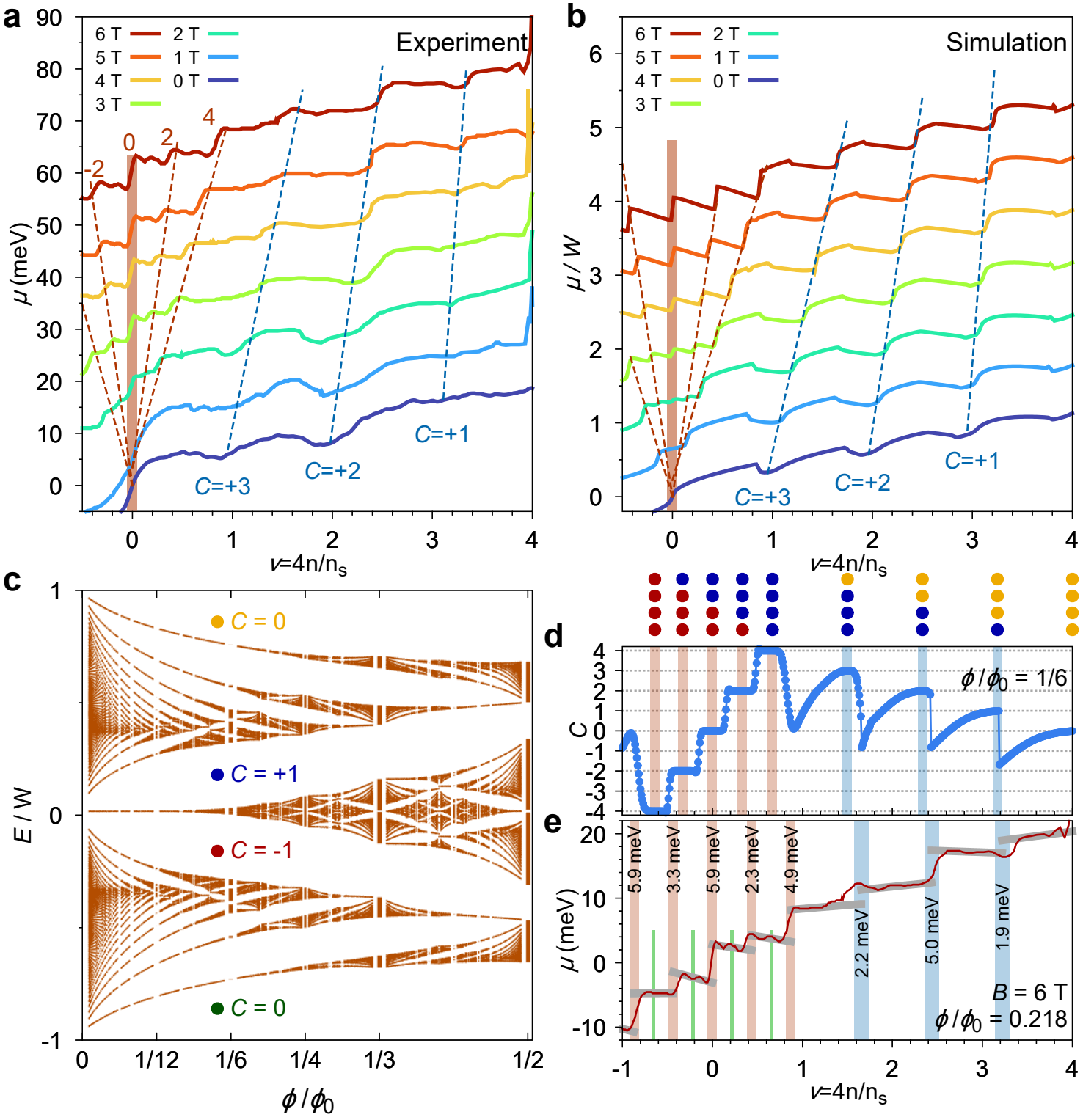
a
Experiment
6 T
5 T
4 T
3 T
2 T
1 T
0 T
μ (meV)
ν=4n/n_s
-2
0
2
4
C=+3
C=+2
C=+1
b
Simulation
μ / W
c
E / W
C = 0
C = +1
C = -1
C = 0
ϕ / ϕ_0
0
1/12
1/6
1/4
1/3
1/2
d
C
ϕ / ϕ_0 = 1/6
e
μ (meV)
5.9 meV
3.3 meV
5.9 meV
2.3 meV
4.9 meV
2.2 meV
5.0 meV
1.9 meV
B = 6 T
ϕ / ϕ_0 = 0.218

Figure 4

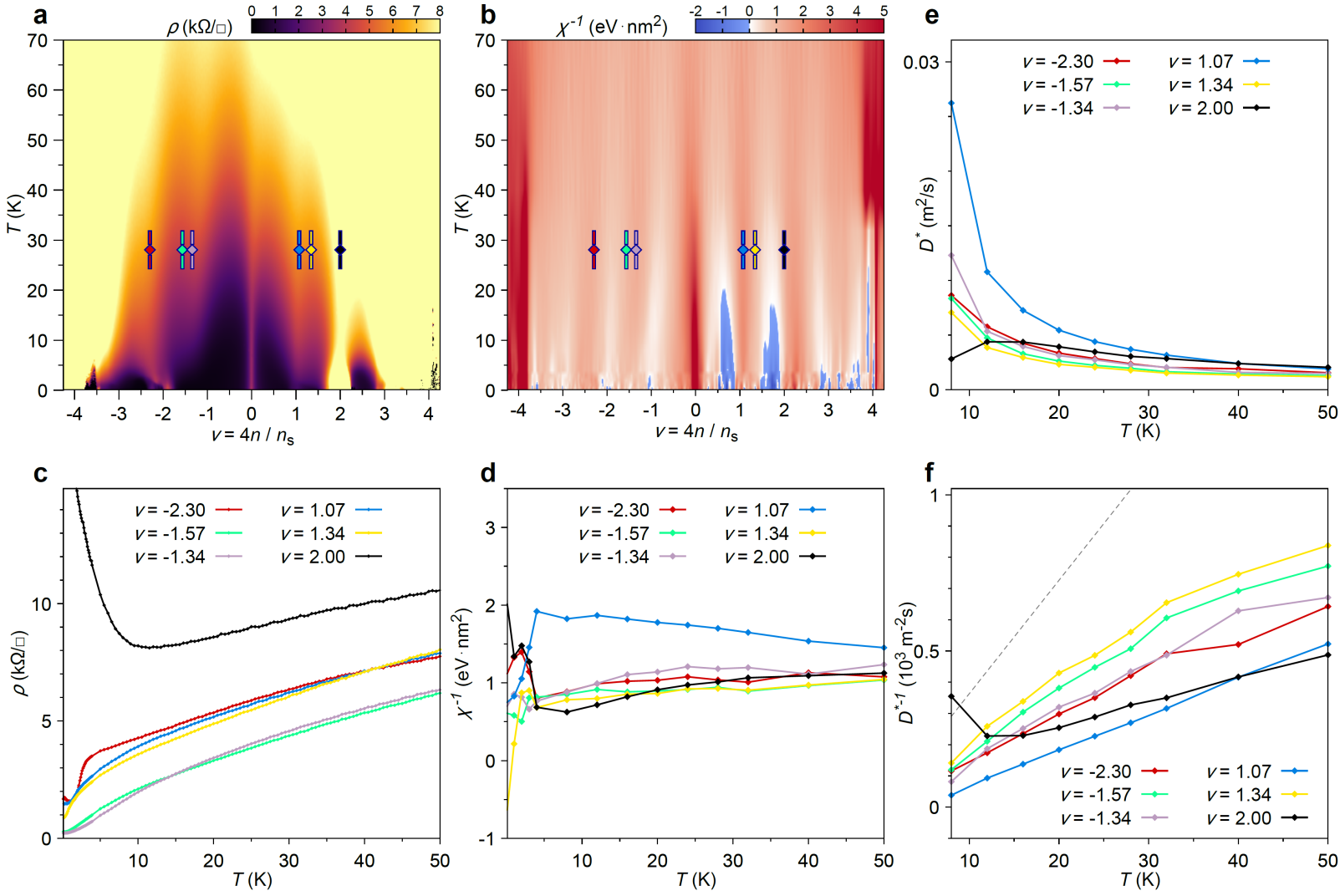
a
ρ (kΩ/□)
0 1 2 3 4 5 6 7 8
T (K)
ν = 4n / n_s
b
χ^-1 (eV·nm^2)
-2 -1 0 1 2 3 4 5
T (K)
ν = 4n / n_s
e
ν = -2.30
ν = -1.57
ν = -1.34
ν = 1.07
ν = 1.34
ν = 2.00
D* (m^2/s)
T (K)
c
ρ (kΩ/□)
T (K)
d
χ^-1 (eV·nm^2)
T (K)
f
D*^-1 (10^3 m^-2 s)
T (K)

Extended Data Figure 1

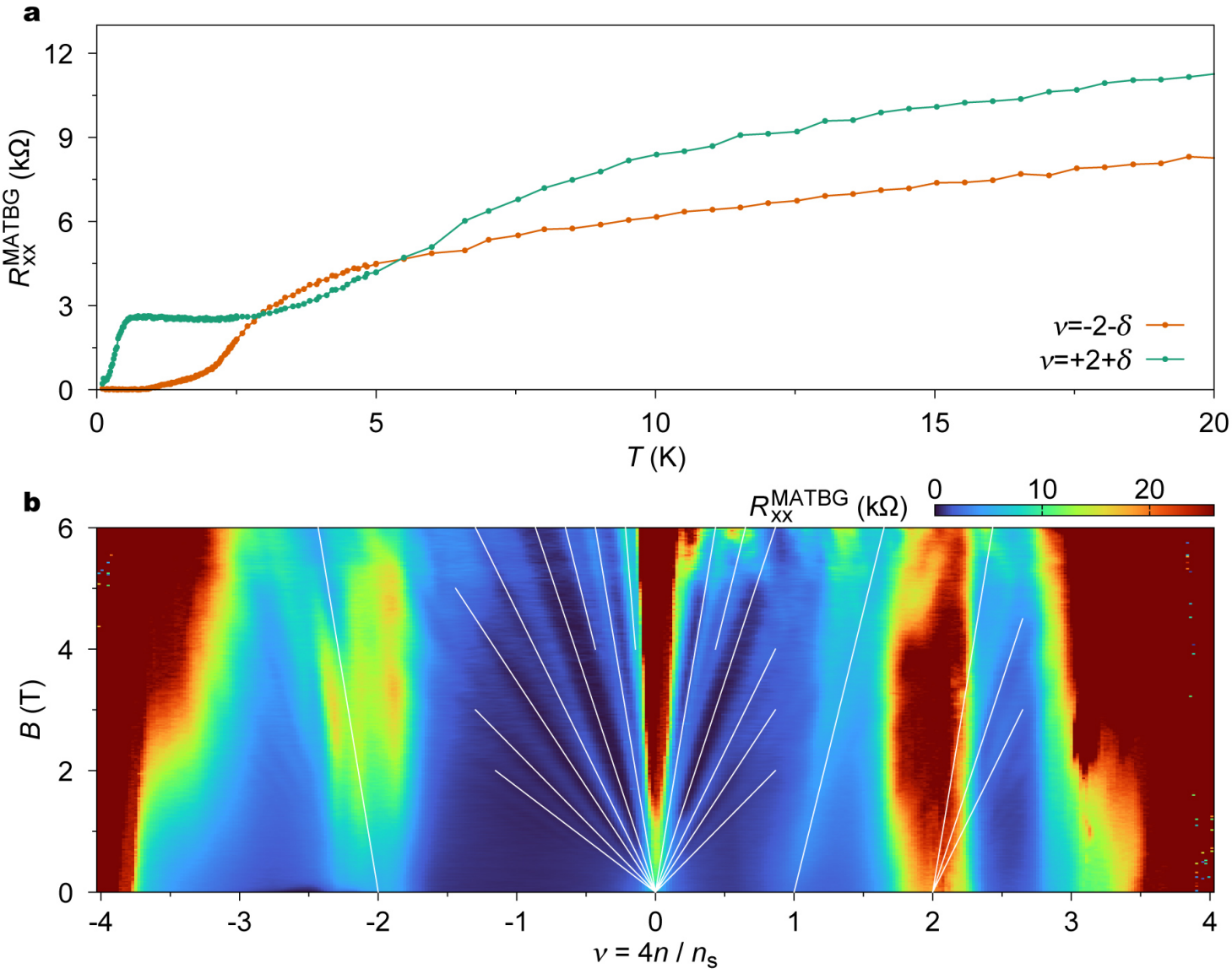

Extended Data Figure 2

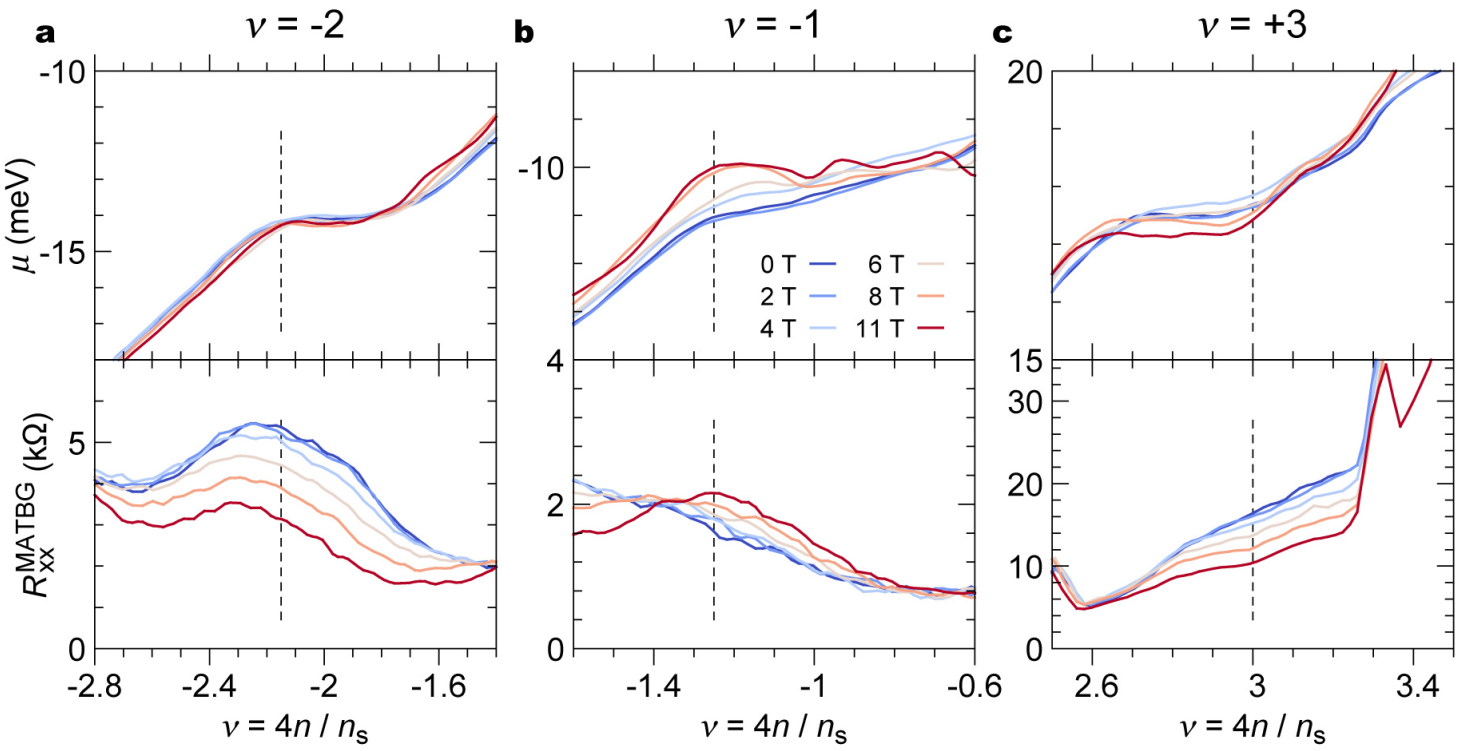

Extended Data Figure 3

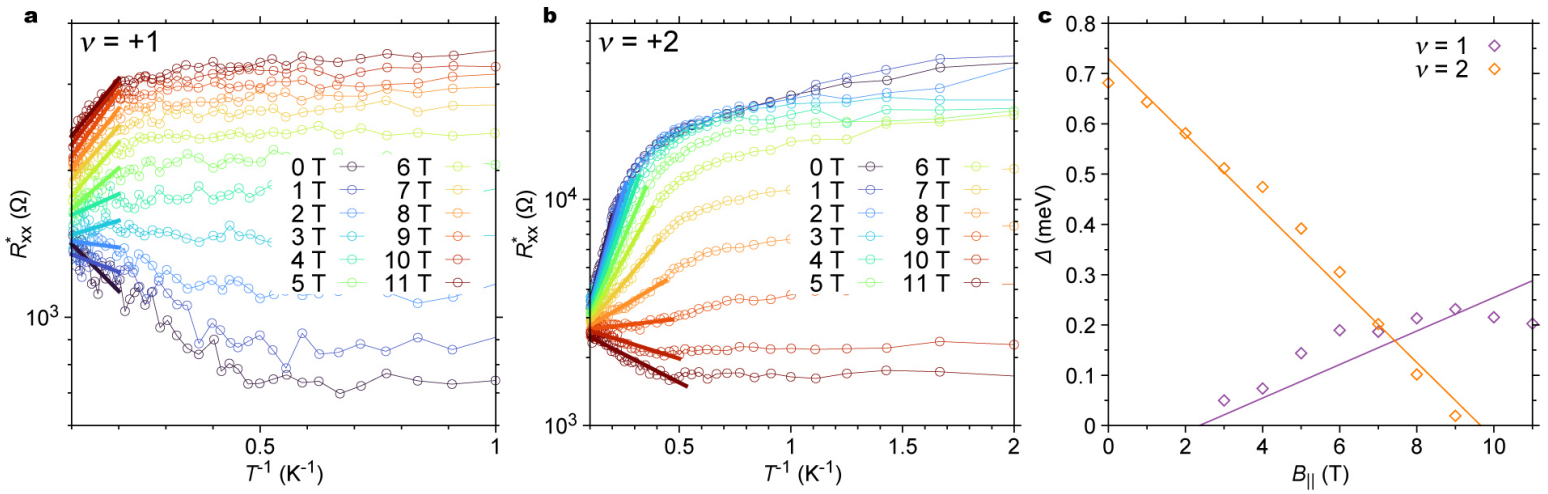

Extended Data Figure 4

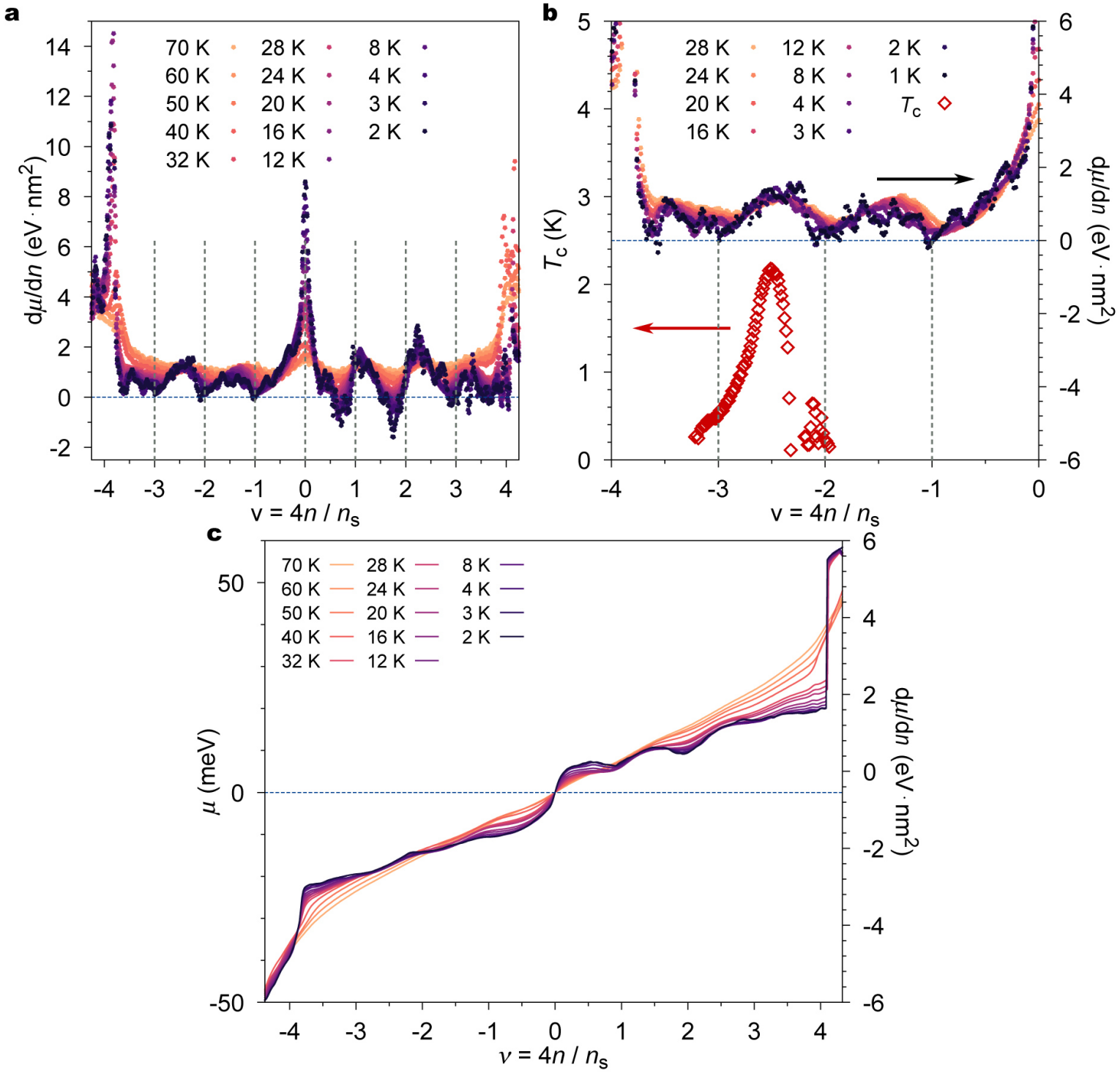

Extended Data Figure 5

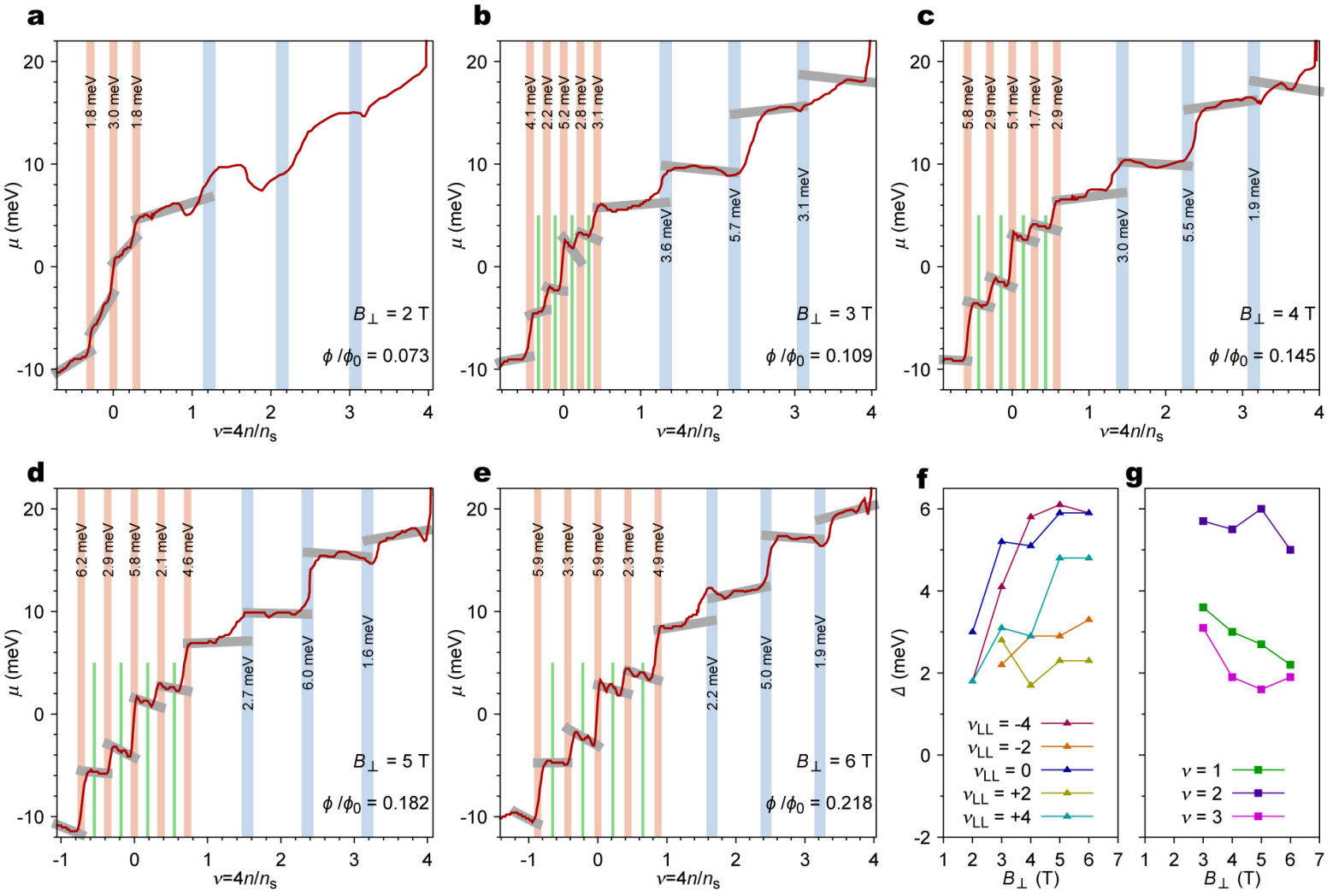

Extended Data Figure 6